JACS
JOURNAL OF THE AMERICAN CHEMICAL SOCIETY

Subscriber access provided by ISTANBUL TEKNIK UNIV

Article

A Nickel Hydride Complex in the Active Site of Methyl-Coenzyme M Reductase: Implications for the Catalytic Cycle

Jeffrey Harmer, Cinzia Finazzo, Rafal Piskorski, Sieglinde Ebner, Evert C. Duin, Meike Goenrich, Rudolf K. Thauer, Markus Reiher, Arthur Schweiger, Dariush Hinderberger, and Bernhard Jaun

J. Am. Chem. Soc., **2008**, 130 (33), 10907-10920 • DOI: 10.1021/ja710949e • Publication Date (Web): 25 July 2008

Downloaded from http://pubs.acs.org on February 8, 2009

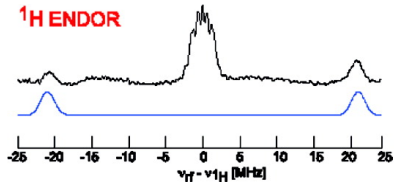

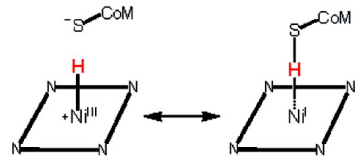

More About This Article

Additional resources and features associated with this article are available within the HTML version:

- Supporting Information
- Links to the 1 articles that cite this article, as of the time of this article download
- Access to high resolution figures
- Links to articles and content related to this article
- Copyright permission to reproduce figures and/or text from this article

View the Full Text HTML

ACS Publications
High quality. High impact.

Journal of the American Chemical Society is published by the American Chemical Society. 1155 Sixteenth Street N.W., Washington, DC 20036

J|A|C|S
ARTICLES

Published on Web 07/25/2008

A Nickel Hydride Complex in the Active Site of Methyl-Coenzyme M Reductase: Implications for the Catalytic Cycle

Jeffrey Harmer,*,†,‡ Cinzia Finazzo,‡ Rafal Piskorski,§ Sieglinde Ebner,§ Evert C. Duin,⊥ Meike Goenrich,|| Rudolf K. Thauer,|| Markus Reiher,‡ Arthur Schweiger,‡ Dariush Hinderberger,‡,# and Bernhard Jaun*,§

Centre for Advanced Electron Spin Resonance, Department of Chemistry, University of Oxford, South Parks Road, OX1 3QR, Oxford, United Kingdom, Laboratory of Physical Chemistry, ETH Zurich, 8093 Zurich, Switzerland, Laboratory of Organic Chemistry, ETH Zurich, 8093 Zurich, Switzerland, Max Planck Institute for Terrestrial Microbiology, Department of Biochemistry, Karl-von-Frisch Strasse, 35043 Marburg, Germany, and Department of Chemistry and Biochemistry, Auburn University, Alabama 36849-5312

Received December 9, 2007; E-mail: jaun@org.chem.ethz.ch; jeffrey.harmer@chem.ox.ac.uk

Abstract: Methanogenic archaea utilize a specific pathway in their metabolism, converting C_1 substrates (i.e., CO_2) or acetate to methane and thereby providing energy for the cell. Methyl-coenzyme M reductase (MCR) catalyzes the key step in the process, namely methyl-coenzyme M (CH_3-S-CoM) plus coenzyme B (HS-CoB) to methane and CoM-S-S-CoB. The active site of MCR contains the nickel porphinoid F_{430}. We report here on the coordinated ligands of the two paramagnetic MCR_{red2} states, induced when HS-CoM (a reversible competitive inhibitor) and the second substrate HS-CoB or its analogue CH_3-S-CoB are added to the enzyme in the active MCR_{red1} state ($Ni^{I}F_{430}$). Continuous wave and pulse EPR spectroscopy are used to show that the MCR_{red2a} state exhibits a very large proton hyperfine interaction with principal values $A(^1H) = [-43,-42,-5]$ MHz and thus represents formally a $Ni^{III}F_{430}$ hydride complex formed by oxidative addition to Ni^{I}. In view of the known ability of nickel hydrides to activate methane, and the growing body of evidence for the involvement of MCR in "reverse" methanogenesis (anaerobic oxidation of methane), we believe that the nickel hydride complex reported here could play a key role in helping to understand both the mechanism of "reverse" and "forward" methanogenesis.

Introduction

Methanogenic archae utilize a specific pathway in their metabolism, converting C_1 substrates or acetate to methane and thereby providing energy for the cell.[1] In the reaction $CO_2 + 8H \rightarrow 2H_2O + CH_4$, the overall 8e reduction of CO_2 occurs via four 2e steps while the C_1 carbon fragment is being bound to a series of coenzymes. Methyl-coenzyme M reductase (MCR) catalyzes the key and last step of methanogenesis in archaea, namely the reduction of methyl-coenzyme M (CH_3-S-CoM, 2-(methylthio)ethane sulfonate) with coenzyme B (HS-CoB, 7-thioheptanoyl-threoninephosphate) to methane and the heterodisulfide CoM-S-S-CoB, which is the methane forming step in the energy metabolism of all methanogenic archaea. MCR contains bound 2 mol of the nickel porphinoid cofactor F_{430} as the prosthetic group[2–4] which has to be in the Ni(I) oxidation state for the enzyme to be active.[5]

$$CH_3\text{-S-CoM} + \text{HS-CoB} \rightarrow CH_4 + \text{CoM-S-S-CoB} \qquad \Delta G^{\circ\prime} = 30 \pm 10 \text{ kJ/mol} \quad (1)$$

Several crystal structures of MCR in an inactive state (Ni(II), d^8, $S = 1$) have been determined.[6–9] The enzyme has an interlinked $\alpha_2\beta_2\gamma_2$ subunit structure with two F_{430} molecules in two active sites that are 5.1 nm apart. Each F_{430} is buried deep within the protein and is accessible from the outside via a 5 nm long channel, through which CH_3-S-CoM can diffuse to reach F_{430}. The channel is designed such that the terminal group of the heptanoyl arm of coenzyme B remains 0.8 nm from the nickel. CH_3-S-CoM can bind in the pocket close to F_{430} such

† University of Oxford.
‡ Laboratory of Physical Chemistry, ETH Zurich.
§ Laboratory of Organic Chemistry, ETH Zurich.
⊥ Auburn University.
|| Max Planck Institute for Terrestrial Microbiology.
Max Planck Institute for Polymer Research, Ackermannweg 10, 55128 Mainz, Germany.

(1) Thauer, R. K. *Microbiology* **1998**, *144*, 2377–2406.
(2) Ellefson, W. L.; Whitman, W. B.; Wolfe, R. S. *Proc. Natl. Acad. Sci. U.S.A.* **1982**, *79*, 3707–3710.
(3) Pfaltz, A.; Jaun, B.; Faessler, A.; Eschenmoser, A.; Jaenchen, R.; Gilles, H. H.; Diekert, G.; Thauer, R. K. *Helv. Chim. Acta* **1982**, *65*, 828–865.
(4) Jaun, B.; Pfaltz, A. *J. Chem. Soc., Chem. Commun.* **1986**, *17*, 1327–1329.
(5) Goubeaud, M.; Schreiner, G.; Thauer, R. K. *Eur. J. Biochem.* **1997**, *243*, 110–114.
(6) Ermler, U.; Grabase, W.; Shima, S.; Goubeaud, M.; Thauer, R. K. *Science* **1997**, *278*, 1457–1462.
(7) Shima, S.; Goubeaud, M.; Vinzenz, D.; Thauer, R. K.; Ermler, U. J. *Biochemistry* **1997**, *121*, 829–830.
(8) Grabarse, W.; Mahlert, F.; Shima, S.; Thauer, R. K.; Ermler, U. *J. Mol. Biol.* **2000**, *303*, 329–344.
(9) Grabarse, W.; Mahlert, F.; Shima, S.; Duin, E. C.; Goubeaud, M.; Sima, S.; Thauer, R. K.; Lamzin, V.; Ermler, U. *J. Mol. Biol.* **2001**, *309*, 315–330.

 © 2008 American Chemical Society

that the thioether S is positioned above the nickel. The available crystal structures differ in the ligands axially bound to F_{430}. All structures have the oxygen of the α′-glutamine residue 147 coordinated axially from the distal face to the nickel ion. MCR_{silent} coordinates a sulfonate oxygen of CoM-S-S-CoB, and $MCR_{ox1\text{-}silent}$ has the thiol(ate) sulfur of coenzyme M (HS-CoM) coordinated to the Ni^{II} ion (Scheme 1 and Table 1).

Currently two main cataylic mechanisms are proposed for eq 1, both of which start with $Ni^{I}F_{430}$. In mechanism A,[2,5,10–14] the crucial step is a methyl transfer from CH_3-S-CoM to $Ni^{I}F_{430}$, yielding a $CH_3{-}Ni^{III}F_{430}^{+}$ compound. This step is then followed by protonolysis to yield methane and CoM-S-S-CoB. Alkyl− and $CH_3{-}Ni^{III}F_{430}^{+}$ complexes have been generated by the addition of $Br(CH_2)_3SO_3^{-}$,[15,16] $BrCH_3$,[17] or ICH_3[18] to MCR in the enzymatically active Ni^{I} oxidation state. In these experiments a Ni−C coordination was proved by EPR spectroscopy with the spin population on the carbon atom being ca. $\eta_C = 0.09$. In mechanism B,[19,20] a proposal based on DFT calculations, $Ni^{I}F_{430}$ reacts with CH_3-S-CoM to give a $Ni^{II}F_{430}$ thiolate and a free $^{\bullet}CH_3$ radical that is immediately quenched by H-atom transfer from HS-CoB.

Active MCR (red1 states) exhibits axial EPR spectra characteristic of a d^9, $S = {}^1/_2$, Ni^{I} complex with the unpaired electron in an orbital with predominately $d_{x^2-y^2}$ character.[4,21–25] MCR_{red1} states are formed when the gas mixture normally used for cell growth (80% H_2/20% CO_2) is made more reducing (100% H_2) before harvesting the cells.[26,27] Upon addition of the two substrates CH_3-S-CoM and HS-CoB no direct intermediates can be observed and characterized, presumably because either a conformational change associated with HS-CoB binding or the first chemical reaction step is rate limiting. However, potentially good models for the coordination of CH_3-S-CoM to nickel and the binding of HS-CoB to the protein can be obtained with the substrate analogue HS-CoM (a competitive inhibitor to CH_3-S-CoM) and HS-CoB. As we have recently found in a high-field electron paramagnetic resonance (EPR) study,[28] the addition of the second substrate HS-CoB to the MCR_{red1c} preparation (MCR_{red1a} + HS-CoM, MCR_{red1a} denotes $Ni^{I}F_{430}$ in the absence of substrates) induces two states at the expense of the MCR_{red1c} state that we have designated MCR_{red2a}[28] and MCR_{red2r},[21] after their axial and rhombic EPR spectra, respectively. This induction is presumably triggered by a conformational change of the MCR_{red1c} state when HS-CoB binds and may therefore mimic a potential conformation that could result in S−C bond activation when HS-CoB is added to MCR_{red1m} (MCR_{red1a} + CH_3-S-CoM). The amount of MCR_{red1c} conversion is temperature dependent, but under all experimental conditions to date a maximum conversion of only ca. 50% has been achieved.[14,28] This finding may indicate that the two F_{430} molecules of each MCR function as a unit, and a "two-stroke engine" mechanism has been proposed to explain this apparent cooperativity behavior.[14]

The MCR_{red2r} state has a distinctly orthorhombic Ni^{I}-derived EPR spectrum "unusual" for a porphyrinoid ligand. Electron−nuclear double resonance (ENDOR) and hyperfine sublevel correlation spectroscopy (HYSCORE) measurements have shown that there are two types of pyrrole nitrogen nuclei, a set (probably three nuclei) with hyperfine couplings with the range $|A(^{14}N)| = 20-27$ MHz and a second set (probably one nucleus) with a distinctively smaller hyperfine coupling of $|A(^{14}N)| = 12-16$ MHz, indicating a significant electronic and/or geometric distortion of F_{430}.[29] This result is quite distinct in comparison to the MCR_{red1} or MCR_{ox1}[30] states where all four nitrogens have similar hyperfine couplings. Two large isotropic proton couplings were also reported; however, their interpretation was only tentative since without ^2H labeling there are many possible assignments. We have also shown, using labeled $H^{33}S$-CoM, that the thiol(ate) sulfur is coordinated axially to the Ni^{I} ion (Table 1).[31] The coordination environment of $Ni^{I}F_{430}$ in the MCR_{red2a} state is until now unknown.

This study aims at elucidating the coordination geometry of the nickel complexes in the red2a and red2r states and to consider them as potential models for intermediates in the catalytic cycle. We used pulse ENDOR and HYSCORE at different microwave (mw) frequencies to study the hyperfine interactions between the electron spins with the surrounding magnetic nuclei of the ligands. Key proton assignments were obtained with $HS{-}CD_2(CH_2)_2SO_3^{-}$ (denoted [2-$^2H_2$]-HS-CoM), and exchangeable proton signals were assigned by preparing MCR in D_2O. Using these preparations we were able to identify protons with strikingly large hyperfine couplings and determine that MCR_{red2a} contains a nickel hydride complex at the active site.

(10) Jaun, B. *Helv. Chim. Acta* **1990**, *73*, 2209–2217.
(11) Horng, Y.-C.; Becker, D. F.; Ragsdale, S. W. *Biochemistry* **2001**, *40*, 12875–12885.
(12) Ghosh, A.; Wondimagegn, T.; Ryeng, H. *Curr. Opin. Chem. Biol.* **2001**, *5*, 744–750.
(13) Duin, E. C.; Signor, L.; Piskorski, R.; Mahlert, F.; Clay, M. D.; Goenrich, M.; Thauer, R. K.; Jaun, B.; Johnson, M. K. *J. Biol. Inorg. Chem.* **2004**, *9*, 563–576.
(14) Goenrich, M.; Duin, E. C.; Mahlert, F.; Thauer, R. K. *J. Biol. Inorg. Chem.* **2005**, *10*, 333–342.
(15) Goenrich, M.; Mahlert, F.; Duin, E. C.; Bauer, C.; Jaun, B.; Thauer, R. K. *J. Biol. Inorg. Chem.* **2004**, *9*, 691–705.
(16) Hinderberger, D.; Piskorski, R.; Goenrich, M.; Thauer, R. K.; Schweiger, A.; Harmer, J.; Jaun, B. *Angew. Chem., Int. Ed.* **2006**, *45*, 3602–3607.
(17) Yang, N.; Reiher, M.; Wang, M.; Harmer, J.; Duin, E. C. *J. Am. Chem. Soc.* **2007**, *129*, 11028–11029.
(18) Dey, M.; Telser, J.; Kunz, R. C.; Lees, N. S.; Ragsdale, S. W.; Hoffman, B. M. *J. Am. Chem. Soc.* **2007**, *129*, 11030–11032.
(19) Pelmenschikov, V.; Siegbahn, P. E. M. *J. Biol. Inorg. Chem.* **2003**, *8*, 653–662.
(20) Pelmenschikov, V.; Blomberg, M. R. A.; Siegbahn, P. E. M.; Crabtree, R. H. *J. Am. Chem. Soc.* **2002**, *124*, 4039–4049.
(21) (a) Mahlert, F.; Grabarse, W.; Kahnt, J.; Thauer, R. K.; Duin, E. C. *J. Biol. Inorg. Chem.* **2002**, *7*, 101–112. (b) Mahlert, F.; Grabarse, W.; Kahnt, J.; Thauer, R. K.; Duin, E. C. *J. Biol. Inorg. Chem.* **2002**, *7*, 351.
(22) Mahlert, F.; Bauer, C.; Jaun, B.; Thauer, R. K.; Duin, E. C. *J. Biol. Inorg. Chem.* **2002**, *7*, 500–513.
(23) Rospert, S.; Boecher, R.; Albracht, S. P. J.; Thauer, R. K. *FEBS Lett.* **1991**, *291*, 371–375.
(24) Goubeaud, M.; Schreiner, G.; Thauer, R. K. *Eur. J. Biochem.* **1997**, *243*, 110–114.
(25) Rospert, S.; Voges, M.; Berkessel, A.; Albracht, S. P. J.; Thauer, R. K. *Eur. J. Biochem.* **1992**, *210*, 101–107.
(26) Albracht, S. P. J.; Ankel-Fuchs, D.; Böcher, R.; Ellermann, J.; Moll, J.; Van der Zwaan, J. W.; Thauer, R. K. *Biochim. Biophys. Acta* **1988**, *955*, 86–102.
(27) Krzycki, J. A.; Prince, R. C. *Biochim. Biophys. Acta* **1990**, *1015*, 53–60.
(28) Kern, D. I.; Goenrich, M.; Jaun, B.; Thauer, R. K.; Harmer, J.; Hinderberger, D. *J. Biol. Inorg. Chem.* **2007**, *12*, 1097–1105.
(29) Finazzo, C.; Harmer, J.; Jaun, B.; Duin, E. C.; Mahlert, F.; Thauer, R. K.; Van Doorslaer, S.; Schweiger, A. *J. Biol. Inorg. Chem.* **2003**, *8*, 586–593.
(30) Harmer, J.; Finazzo, C.; Piskorski, R.; Bauer, C.; Jaun, B.; Duin, E. C.; Goenrich, M.; Thauer, R. K.; Van Doorslaer, S.; Schweiger, A. *J. Am. Chem. Soc.* **2005**, *127*, 17744–17755.
(31) Finazzo, C.; Harmer, J.; Bauer, C.; Jaun, B.; Duin, E. C.; Mahlert, F.; Goenrich, M.; Thauer, R. K.; Van Doorslaer, S.; Schweiger, A. *J. Am. Chem. Soc.* **2003**, *125*, 4988–4989.

Experimental Section

Protein Purification and Sample Preparation. Methyl-coenzyme M reductase isoenzyme I from *Methanothermobacter marburgensis* was purified as described.[14,21] The enzyme is purified with 10 mM HS-CoM present in all the buffers used. Therefore the obtained enzyme is in the MCR_{red1c} form. The spin concentration per mole of F_{430} was approximately 0.8−0.9. The protein concentration was determined using the method of Bradford[32] with bovine serum albumin (Serva) as a standard or by measuring the absorbance difference of oxidized enzyme (MCR_{silent}) at 420 nm using $\epsilon = 44\,000\ M^{-1}\ cm^{-1}$ for a molecular mass of 280 000 Da. The "MCR_{red1c} + HS-CoB" sample was prepared by adding HS-CoB to the sample to a concentration of 5 mM. The "MCR_{red1c} + CH_3-S-CoB" sample was prepared by adding CH_3-S-CoB to the sample to a concentration of 5 mM. The MCR samples in ^2H_2O were prepared by washing the enzyme preparation extensively with 50 mM TrisHCl (pD 7.6) in ^2H_2O using an Amicon centrifugation cell with a 100 kDa cutoff (Millipore, Bedford MA). The MCR sample with [2-$^2H_2$] HS-CoM was prepared by washing the MCR_{red1c} preparation extensively with a 50 mM TrisHCl (pH 7.6) buffer containing 10 mM [2-$^2H_2$] HS-CoM. In both preparations, the red2 states were induced by addition of HS-CoB to a concentration of 5 mM. The EPR samples were frozen in liquid nitrogen for shipping and storage.

EPR Spectroscopy (Sample Control). As a control of the sample quality and concentration, X-, Q-, and W-band sample tubes were measured by EPR spectroscopy at 77 K with liquid nitrogen in a nitrogen finger Dewar. CW EPR spectra at X-band were recorded with a Bruker EMX-6/1 EPR spectrometer composed of the EMX 1/3 console, an ER 041 X6 bridge with a built-in ER-0410-116 microwave frequency counter, an ER-070 magnet, and an ER-4102st standard universal rectangular cavity. All spectra were recorded with a field modulation frequency of 100 kHz. The EPR spin concentrations were carried out under nonsaturating conditions using 10 mM copper perchlorate as the standard (10 mM CuSO4; 2 M NaClO4; 10 mM HCl).

EPR Spectroscopy. The X- and W-band (9.7/94 GHz) measurements were made on a Bruker E680 spectrometer and at Q-band (34.83 GHz) on a home-built instrument.[33] Both instruments were equipped with a helium gas-flow cryostat from Oxford Inc. The W-band echo-detected EPR spectra were recorded by integrating the echo intensity created with the mw pulse sequence $\pi/2$-τ-π-τ-*echo* with mw pulse lengths $t_{\pi/2} = 100$ ns, $t_\pi = 200$ ns, and $\tau = 500-700$ ns. The first derivative of this spectrum was calculated numerically. The field was calibrated using the two central lines from a CaO sample containing manganese ions. At Q-band (35 GHz) the ^{1}H Davies ENDOR spectra were measured with the mw pulse sequence π-T-$\pi/2$-τ-π-τ-*echo*, with mw pulses of length $t_{\pi/2} = 20$ ns, $t_\pi = 40$ ns, and $\tau = 260$ ns (Figure 2) and mw pulses of length $t_{\pi/2} = 50$ ns, $t_\pi = 100$ ns, and $\tau = 220$ ns (Figures 5 and 6). A radio frequency pulse of length 10 μs and variable frequency ν_{rf} was applied during time T. X-band HYSCORE experiments employed the pulse sequence $\pi/2$-τ-$\pi/2$-t_1-π-t_2-$\pi/2$-τ-*echo* with mw pulses of lengths $t_{\pi/2} = t_\pi = 16$ ns, starting times of 96 ns for t_1 and t_2, $\Delta t = 16$ ns (data matrix 256 × 256). An eight-step phase cycle was used to remove unwanted echoes. The HYSCORE data were processed with MATLAB 7.0 (The MathWorks, Inc.). The time traces were baseline corrected with an exponential, apodized with a Gaussian window and zero filled. After a two-dimensional Fourier transformation absolute-value spectra were calculated. Spectra recorded with different τ values were added to eliminate τ-dependent blind spots.

EPR Simulations. The EPR and Davies ENDOR spectra were simulated with the program EasySpin.[34] HYSCORE spectra were simulated with a program written in-house[35] or, if only the cross-peak frequencies (and not the intensities) were of interest, by exact diagonalization of the spin Hamiltonian. Simulated spectra were generally fitted to experimental spectra using the Newton−Gauss−Levenberg/Marquardt (NGL/M) algorithm, and the Jacobian matrix for the nonlinear parameters (the hyperfine couplings) was calculated numerically. To find the global minimum, the NGL/M algorithm was used in conjunction with a large set of initial guesses, and the best fit was then found. In the case of the ENDOR data for protons H_{ax} and H_{rh}, regions of the spectra not overlapped by other protons only were included (all signals greater ± 6 MHz from the Larmor frequency). For H_{rh}, the smallest principal value ($|A_3| = 5$ MHz), which gives signals that overlap with many other proton signals, was determine uniquely by HYSCORE spectra since the ridges are displaced from the antidiagonal because of the large anisotropy and thus separated from other proton signals. HYSCORE simulations were optimized by adjusting the hyperfine coupling (and nuclear quadrupole) parameters to best match the peak positions (intensities were not included because of the large computational time and limited accuracy of the peak intensity calculation). Protons iso1 and iso2 were fitted by including only the spectral region around their corresponding peaks; the β proton ENDOR simulation parameters were adjusted by hand in conjunction with fits to the ^{2}H/^{1}H HYSCORE spectra until good agreement was obtained.

EPR Theory. The spin Hamiltonian for an $S = {}^1/_2$ system coupled to i nuclei, in frequency units, is given by

$$H = (\beta_e/h)\mathbf{S}\mathbf{g}\mathbf{B}_0 + \sum \mathbf{S}\mathbf{A}_i\mathbf{I}_i - (\beta_n/h)\sum g_{i,n}\mathbf{I}_i\mathbf{B}_0 + \sum \mathbf{I}_i\mathbf{Q}_i\mathbf{I}_i \quad (2)$$

where the terms describe the electron Zeeman interaction, the hyperfine interactions, the nuclear Zeeman interactions, and the nuclear quadrupole interactions (for nuclei with $I > {}^1/_2$).

The ENDOR spectrum of a nucleus with spin $I = {}^1/_2$ at a single orientation consists of two transitions. For $\mathbf{B}_0$ along one of the hyperfine principal axes the frequencies are given by $\nu = |\nu_I \pm {}^1/_2 A_i|$, where ν_I is the nuclear Zeeman frequency and A_i is one of the principal hyperfine values. In a disordered sample the observed spectrum is the sum of a set of weighted orientations. For a nucleus with spin $I = 1$ (^{14}N) there are four single-quantum transitions, for the magnetic field along one of the principal axes the frequencies of the energy levels are given by $\nu = |\nu_I \pm {}^1/_2 A_i + {}^3/_2 Q_i(2m_I + 1)|$, where Q_i denotes a principal value of the $\mathbf{Q}$ tensor along the principal axis and m_I is the nuclear spin quantum number ($m_I = -1, 0, 1$). In HYSCORE, all three nuclear transitions in each electron spin manifold can potentially be observed: two single-quantum (sq) transitions with $|\Delta m_I| = \pm 1$ and one double-quantum (dq) transition with $|\Delta m_I| = \pm 2$. A HYSCORE spectrum contains cross-peaks between the nuclear frequencies in one electron spin manifold with the nuclear frequencies in the other electron spin manifold. Generally, only a few of the possible 9 (3 × 3) cross-peaks are observed.

Density Functional Theory (DFT). Structure optimizations have been carried out with the Turbomole program package[36] employing the density functional BP86[37] (in combination with the resolution-of-the-identity density fitting technique with Karlsruhe auxiliary basis sets[38]). For all calculations the valence-triple-ζ plus polarization basis set TZVP by Schäfer et al.[39] was applied. The EPR parameters, the hyperfine interactions, were calculated with the Amsterdam Density Functional package (ADF 2005.01).[40] The

(32) Bradford, M. M. *Anal. Biochem.* **1976**, *72*, 248–254.
(33) Gromov, I.; Shane, J.; Forrer, J.; Rakhmatoullin, R.; Rozentzwaig, Yu; Schweiger, A. *J. Magn. Reson.* **2001**, *149*, 196–203.
(34) Stoll, S.; Schweiger, A. *J. Magn. Reson.* **2006**, *178*, 42–55.
(35) Madi, Z; Van Doorslaer, S; Schweiger, A. *J. Magn. Reson.* **2002**, *154*, 181–191.
(36) Ahlrichs, R.; Bär, M.; Häser, M.; Horn, H.; Kölmel, C. *Chem. Phys. Lett.* **1989**, *162*, 165–169.
(37) (a) Becke, A. D. *Phys. Rev. A* **1988**, *38*, 3098–3100. (b) Perdew, J. P. *Phys. Rev. B* **1986**, *33*, 8822–8824.
(38) ftp://ftp.chemie.uni-karlsruhe.de/pub/jbasen.
(39) Schäfer, A.; Huber, C.; Ahlrichs, R. *J. Chem. Phys.* **1994**, *100*, 5829.
(40) te Velde, G.; Bickelhaupt, F. M.; van Gisbergen, S. J. A.; Fonseca Guerra, C.; Baerends, E. J.; Snijders, J. G.; Ziegler, T. *J. Comput. Chem.* **2001**, *22*, 931–967.

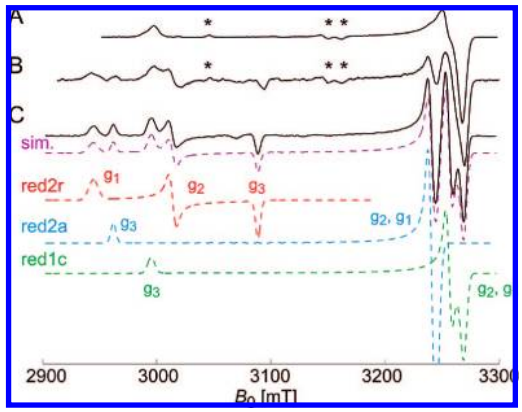

Figure 1. W-band (94.26 GHz) echo-detected EPR spectra (first derivative) measured at 20 K of (A) MCR_{red1c}, (B) MCR_{red1c} + HS-CoB, and (C) MCR_{red1c} + CH_3-S-CoB. Simulations for (C) are shown by the dashed lines, the total (sim.) which comprises the components MCR_{red2r} (17%), MCR_{red2a} (27%), and MCR_{red1c} (56%). In (A and B) an impurity from an ox state of MCR is indicated with an "*".

functional RPBE[41] with the relativistic scalar zeroth-order regular approximation (ZORA)[42] was employed. The calculation was spin-unrestricted with a Slater-type basis set of triple-ζ quality with two polarization functions (TZ2P) with no frozen cores.

Results

Figure 1 shows W-band (mw frequency 94.26 GHz) EPR spectra from (A) MCR_{red1c} (MCR_{red1a} + HS-CoM), (B) MCR_{red1c} + HS-CoB, and (C) MCR_{red1c} + CH_3-S-CoB and a simulation that comprises the states MCR_{red1c} (56%), MCR_{red2a} (27%), and MCR_{red2r} (17%). Both (B) and (C) show that addition of either HS-CoB or CH_3-S-CoB to MCR_{red1c} induces red2a and red2r signals with very similar g-values, although the relative percentages are different (see Table 2). As expected MCR_{red1c} is still present after addition of either HS-CoB or CH_3-S-CoB, since at most ca. 50% of MCR_{red1c} can be converted into MCR_{red2r}/MCR_{red2a}.[14,28] The MCR_{red1c} signals both before and after addition of HS-CoB or CH_3-S-CoB are very similar.

Proton Interactions. Figure 2 shows the proton region of Q-band (mw frequency of 34.65 GHz) Davies ENDOR spectra from the sample MCR_{red1a} + HS-CoM + HS-CoB, along with the corresponding simulations for the two strongest coupled protons, one from the state MCR_{red2r} (red lines, labeled H_{rh}) and one from MCR_{red2a} (blue lines, labeled H_{ax}). ENDOR results from the sample MCR_{red1a} + HS-CoM + CH_3-S-CoB are virtually identical (Figure S1).

ENDOR spectra measured at the field positions A−I in Figure 2 contain contributions from MCR_{red2r}, spectra B−M contain contributions from MCR_{red2a}, and spectra D−N contain contributions from MCR_{red1c}. Thus, the ENDOR spectrum measured at position A exhibts a pure MCR_{red2r} signal, and the ENDOR spectrum at N is a pure MCR_{red1c} signal. ENDOR spectrum M displays a strikingly large proton coupling of ca. $|A_{ax}(^1H)| =$ 42−43 MHz, which disappears when moving to field position N, allowing it to be definitively assigned to the state MCR_{red2a}. In moving to lower fields, this proton coupling becomes rapidly smaller which indicates a hyperfine interaction with a very large anisotropy. Table 3 lists the proton hyperfine interaction for MCR_{red2a} used to simulate the field dependent data from B−M, $A_{ax}(^1H) = [-43,-42, -5]$ MHz $= -30 + [-13, -12, 25]$ MHz.[43] The largest principal value of the dipolar part is closely orientated along $\mathbf{g}_3$ (Scheme 1 or 2). The negative sign is based on the general form of a dipolar interaction (−1,−1,+2) and DFT calculations (see below). A large proton hyperfine interaction assigned to the MCR_{red2r} state is also observed and was simulated with the hyperfine interaction $A_{rh}(^1H) = \pm[29, 26, 5]$ MHz $= \pm(-20 + [-9, -6, 15])$ MHz (absolute sign unknown); the largest principal value of the dipolar part is orientated approximately between the $\mathbf{g}_1$ and $\mathbf{g}_2$ axes and inclined at 120° to the $\mathbf{g}_3$ axis (Scheme 3). These two strikingly large proton hyperfine interactions were also verified by X-band ENDOR (Figure S2) and HYSCORE data (Figure S3).

Both protons H_{ax} and H_{rh} are exchangeable as shown by the appearance of ^2H signals in MCR samples prepared in ^2H_2O. Figure 3 shows X-band HYSCORE spectra measured at two field positions corresponding to (A) the g_1 position of MCR_{red2r} and (B) the $g_{1,2}$ observer position of MCR_{red2a}. The corresponding deuterium simulation for proton H_{rh}, obtained by scaling the hyperfine interaction given in Table 3 by 6.5144 [$=g_n(^1H)/g_n(^2H)$] and adding the nuclear quadrupole interaction, is given. The good correspondence of the simulated peak positions using the scaled proton hyperfine interactions leaves no doubt that the protons H_{ax} and H_{rh} are exchangeable. The magnitude of the deuterium nuclear quadrupole coupling constant $|e^2qQ/h|$ for both H_{ax} and H_{rh} is ca. <400 kHz (Table 3) and indicates that neither H_{ax} nor H_{rh} is a hydrogen atom in a C−H bond (values are typically <200 kHz).

In particular the very large dipolar part and orientation of the ^1H hyperfine interaction of MCR_{red2a} indicates that the proton is bound axially to the Ni ion and, thus, is a hydride complex; in the MCR_{red2r} state the exchangeable proton H_{rh} is clearly very close to the paramagnetic center (i.e., <0.225 nm) and certainly tilted away from the axial position by ∼120°. Details are given in the discussion section where a number of structures for both species are considered.

Position of HS-CoM. To gain information on the position of HS-CoM, samples were prepared with [2-$^2H_2$]-2-mercaptoethanesulfonate in which the β protons were replaced by deuterium (denoted as [2-$^2H_2$] HS-CoM). First, we present data for MCR_{red2r} (induced with [2-$^2H_2$] HS-CoM). Figure 4A shows the deuterium region of an X-band HYSCORE spectrum which was recorded at the extreme low field end of the EPR spectrum where only MCR_{red2r} signals contribute (g_1 observer position). The simulation which includes both β protons is also displayed. The antidiagonal line drawn at the ^2H Larmor frequency ($\nu(^2H)$ = 2.0 MHz) identifies single-quantum (sq) cross-peaks, and the antidiagonal line at $2 \times \nu(^2H)$ identifies double-quantum[44] (dq) cross-peaks. Examination of the sq region of Figure 4A reveals that two nuclei, $\beta1$ and $\beta2$, contribute to the pattern. Nucleus $\beta1$ manifests itself as two long ridges on either side of the diagonal which run parallel to the antidiagonal from 1.1−2.0 MHz and 2.1−3.0 MHz and are split by the nuclear quadrupole interaction. Nucleus $\beta2$ has a significantly smaller hyperfine coupling and unresolved nuclear quadrupole splittings. This produces an intense peak on either side of the diagonal, which extends along the antidiagonal from 1.3−1.7 MHz and 2.3−2.7 MHz. The dq ridges from 2.6−3.5 MHz and 4.6−5.5 MHz,

(41) Hammer, B.; Hansen, L. B.; Norskov, J. K. *Phys. Rev.* **1999**, *B59*, 7413.
(42) van Lenthe, E.; Baerends, E. J.; Snijders, J. G. *J. Chem. Phys.* **1993**, *99*, 4597.
(43) Isotropic hyperfine coupling $a_{iso} = (A_1 + A_2 + A_3)/3$, dipolar part $[T_1, T_2, T_3] = [A_1, A_2, A_3] - a_{iso}$.
(44) Deuterium with a nuclear spin $I = 1$ has two single-quantum transitions with $\Delta m_I = \pm1$ and one double-quantum transition with $\Delta m_I = \pm2$.

Table 1. Classification of Relevant Paramagnetic States of MCR

Enzyme Form	Structure	g_1,g_2,g_3 values	Description
MCR_{silent}	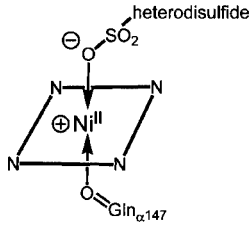	-	Enzyme form purified from cells grown under regular condition with 80% H_2/20% CO_2 as growth gas. Crystal structure solved (6).
MCR_{ox1}	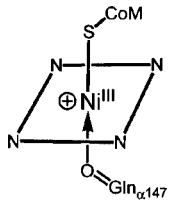	2.231,2.168,2.153	Name derived from the fact that this form can be induced in whole cells by changing the gas phase to 80% N_2/20% CO_2, which represents a more oxidizing condition for the cell (26,74). Structure derived from X-ray absorption (XAS) (75, 76) cryoreduction (77) and ENDOR experiments (30). Can be formed *in vitro* by incubating MCR_{red2} with polysulfide (22). Can be converted into MCR_{red1} by incubation with Ti(III) citrate (24).
$MCR_{ox1\text{-}silent}$	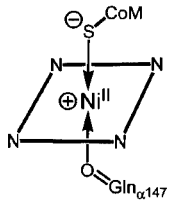	-	Exposure of MCR_{ox1} to oxygen will result in the very slow conversion into $MCR_{ox1\text{-}silent}$. Crystal structure solved (6).
MCR_{red1} Subforms: MCR_{red1a} MCR_{red1c} MCR_{red1m}	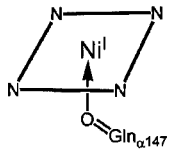	red1a: 2.061,2.064,2.243 red1c: 2.063,2.068,2.248 red1m: 2.061,2.071,2.251	Active form of the enzyme. Structure derived from XAS (75). This enzyme form is very unstable, but activity is retained for extensive periods when either coenzyme M or methyl-coenzyme M are present (21). Therefore three sub forms are distinguished: MCR_{red1a}, for red1 in the ***a***bsence of either compound. MCR_{red1c}, for red1 + coenzyme M present. MCR_{red1m}, for red1 + ***m***ethyl-coenzyme M present.
MCR_{red2} Subforms: MCR_{red2a} MCR_{red2r}	this work 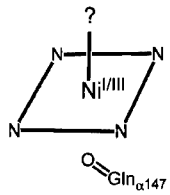	MCR_{red2a}: 2.073,2.077,2.273 MCR_{red2r}: 2.175,2.231,2.288	MCR_{red1} can be converted into the MCR_{red2} form by the addition of coenzyme M and coenzyme B. Two different forms can be recognized that can be interconverted by changing the temperature from 20 °C to 65 °C and vice versa (14, 28). The name of the sub forms is derived from the shape of the EPR signal, being ***a***xial for MCR_{red2a} and ***r***hombic for MCR_{red2r}. In the case of MCR_{red2r} it was shown that the thiol sulfur of coenzyme M is coordinated to the nickel (29, 31). The $MCR_{red2a/r}$ forms are the topic of this paper.

which are shifted behind the antidiagonal line at $2 \times \nu(^2H)$, belong to nucleus $\beta1$ with the largest hyperfine coupling. The shift of the ridges from this antidiagonal is a sensitive measure of the dipolar part of the hyperfine interaction (as the nuclear quadrupole interaction is small) and is well accounted for by the hyperfine interaction determined for $\beta1$. The data quality was further improved by comparing Q-band Davies ENDOR spectra (Figure 5) measured at the g_1 field position of MCR_{red2r}

Table 2. Amplitudes (*A*%) and *g*-Values for the Three States in $MCR_{red1/red2}$ Samples Prepared with HS-CoB or CH_3-S-CoB

preparation	state	*A*%	g_1, g_2, g_3[a]
MCR_{red1a} + HS-CoM + HS-CoB	red1c	69	2.0598, 2.0671, 2.2467
	red2a	14	2.0731, 2.0771, 2.2727
	red2r	17	2.2885, 2.2339, 2.1771
MCR_{red1a} + HS-CoM + CH_3-S-CoB	red1c	56	2.0595, 2.0677, 2.2479
	red2a	27	2.0743, 2.0777, 2.2730
	red2r	17	2.2886, 2.2339, 2.1797

[a] Error in principle values: $\Delta g_i = 0.0005$.

from samples prepared with HS-CoM (A) and [2-$^2H_2$] HS-CoM (B). The differences between spectra (A) and (B) in Figure 5 give directly signals from the β protons of HS-CoM, which are well accounted for by the simulations (Figure 5C) for the β protons using the parameters in Table 3. X-band ^{1}H HYSCORE spectra were also recorded at the low field position of the MCR_{red2r} spectrum to improve confidence in the determined hyperfine couplings (see Figure S4). In addition both spectra, Figure 5A and B, are distinguished by two sets of intense narrow peaks (see also Figure 2), labeled iso1 and iso2, which clearly do not belong to either the β protons of HS-CoM or an exchangeable proton (spectrum not shown). These peaks are further examined in Figure 6 (see below).

Figure 4B shows an X-band HYSCORE spectrum measured at a field position where there are only signals from the states MCR_{red2r}/MCR_{red2a} (no MCR_{red1c} signals). The insets in Figure 4B and C show the EPR spectrum and simulations for the three states so that the contributions to the HYSCORE spectrum are evident. Comparing spectrum (B) with (A) (pure MCR_{red2r} signals), it can be seen that new peaks appear with a smaller hyperfine interaction (closer to the positions where the ^{2}H antidiagonal line intersects with the diagonal line). These signals are therefore assigned to β nuclei from the state MCR_{red2a} which indicates that HS-CoM is relatively close to the Ni ion of F_{430} (i.e., close to the paramagnetic center). HYSCORE spectrum (C) is recorded at the extreme high field end of the $MCR_{red1/red2}$ EPR spectrum where only MCR_{red1c} contributes, and the ^{2}H signals thus also indicate that HS-CoM is relatively close to the Ni ion of F_{430} in the MCR_{red1c} state. It is however not possible to accurately determine the hyperfine interactions from the individual states MCR_{red1c} and MCR_{red2a} since at all other field positions their EPR spectra (thus also the HYSCORE signals) overlap. From the dependence of the ^{2}H HYSCORE signals on the measurement field (Figure S5) an estimate of the largest β proton hyperfine interaction in MCR_{red1c} and/or MCR_{red2a} can be obtained; a dipolar coupling exists with $A_{\beta,max}(^1H) \approx [-2,-2,4]$ MHz, and the axis of the largest principal value points ca. 45° from the $\mathbf{g}_3$ axis. It is clear that the hyperfine interactions to the β protons in the states MCR_{red1c} and MCR_{red2a} are weaker than that in the MCR_{red2r} state, implying an increase in the β proton−electron distances. Note also that our sensitivity at Q-band (where the *g*-value resolution is better) was insufficient to directly measure the ^{2}H interactions with the paramagnetic center via ENDOR.

Previously we reported that MCR_{red2r} has two sets of quasi isotropic proton hyperfine interactions, iso1 and iso2.[29] In Figure 6 these signals are examined in detail with Davies ENDOR spectra recorded at eight field positions across the $MCR_{red1/red2}$ EPR spectrum where MCR_{red2r} is present. These signals persist in samples prepared in ^2H_2O or induced with [2-$^2H_2$] HS-CoM. The dashed lines in Figure 6 follow the field dependence of the *iso1* and *iso2* peaks and show that both hyperfine couplings have a small anisotropy with a similar field dependency. The

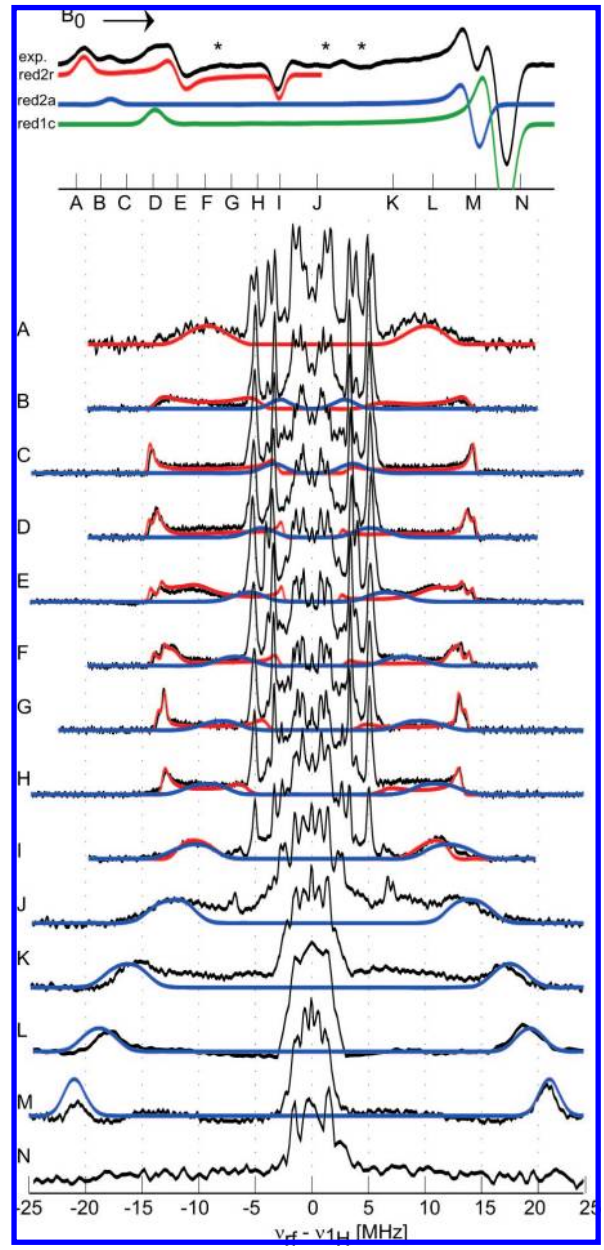

Figure 2. Proton region of Q-band (34.65 GHz) Davies ENDOR spectra measured at 20 K from the sample preparation MCR_{red1a} + HS-CoM + HS-CoB. Experimental, black; simulations for H_{rh} (MCR_{red2r}), red; H_{ax} (MCR_{red2a}), blue. Inset (top): EPR spectrum, black; simulations for MCR_{red2r}, red; MCR_{red2a}, blue; MCR_{red1c}, green; features from ox impurities are indicated with *. The observer positions of the ENDOR spectra are indicated by the letters A to N (corresponding field positions 1076 mT (A), 1082 mT, 1090 mT, 1097 mT, 1104 mT, 1112 mT, 1119 mT, 1127 mT,1133 mT,1143 mT,1164 mT,1176 mT,1188 mT, 1201 mT (N)).

hyperfine coupling for both *iso1* and *iso2* is largest at approximately the field position of g_2, with the coupling at both g_1 and g_3 being smaller and approximately the same. We thus estimate that both hyperfine interactions are approximately axial with principal values of $|A_{iso1}(^1H)| = [10.0, 10.5, 9.9]$ MHz and $|A_{iso2}(^1H)| = [6.7, 7.0, 6.5]$ MHz. These two couplings could potentially stem from the α-protons of HS-CoM, or nonexchangeable protons in the macrocycle of F_{430}, the α′-glutamine residue 147, or the two tyrosine residues of MCR near F_{430}.

Nitrogen Interactions. Signals from weakly coupled nitrogen(s) were investigated with the aim of potentially characterizing the coordination, or otherwise, of the $Gln^{\alpha'147}$ carboxamide

Table 3. ^{1}H Hyperfine and ^{2}H Nuclear Quadrupole Parameters and Error Estimates (Δ) for MCR_{red2a} and MCR_{red2r} States Induced with HS-CoB

nucleus/ comment	A_1, A_2, A_3 ($\Delta A_1, \Delta A_2, \Delta A_3$) [MHz]	α, β, γ[a] (Δα, Δβ, Δγ)	$\lvert e^2qQ/h\rvert$[b] (Δ) [MHz]	η[b] Δη	α, β, γ[a] (Δα, Δβ, Δγ)
		MCR_{red2a}			
H_{ax}, hydride	−43, −42, −5 (1, 1, 2)	−, 5, − (−, 5, −)	<0.4	–	–
		MCR_{red2r}			
H_{rh}	29, 26, 5 [d] (1, 2, 1)	−80, 120, 45 (30, 10, 10)	0.35 (0.05)	0.1 (0.1)	−45, 35, 70 (30, 10, 30)
β_1-HS-CoM	−11.5, −11.5, −0.3 (0.5, 2, 0.5)	−, 135, 230[c] (−, 10, −)	0.2 (0.05)	0.2 (0.1)	140, 45, − (−, 30, −)
β_2-HS-CoM	−8.1, −7.9, −2.6 (0.5, 2, 0.5)	−, 25, 170 [c] (−, 10, −)	0.15 (0.05)	0.2 (0.1)	96, 147, − (−, 30, −)
iso1	10.0, 10.5, 9.9 [d]	0, 0, 0	–	–	–
iso2	6.7, 7.0, 6.5 [d]	0, 0, 0	–	–	–

[a] Euler angles define the passive rotation of the hyperfine or nuclear quadrupole principal axis system into the g-matrix principal axis system, $A = \mathbf{R}(\alpha,\beta,\gamma)A_{diagonal}\mathbf{R}^{\dagger}(\alpha,\beta,\gamma)$. [b] Nuclear quadrupole interactions $\kappa = e^2qQ/(h4I(2I-1))$ and asymmetry parameters $\eta = (Q_x - Q_y)/Q_z$ with $Q_x = -\kappa(1-\eta)$, $Q_y = -\kappa(1+\eta)$, and $Q_z = 2\kappa$. [c] Several values of γ (α) give similar simulations; no error estimate is given. [d] Absolute sign of interaction unknown.

Scheme 1. Nickel Porphyrinoid Cofactor F430 (Absorption Maximum at 430 nm) Responsible for MCR Activity[a]

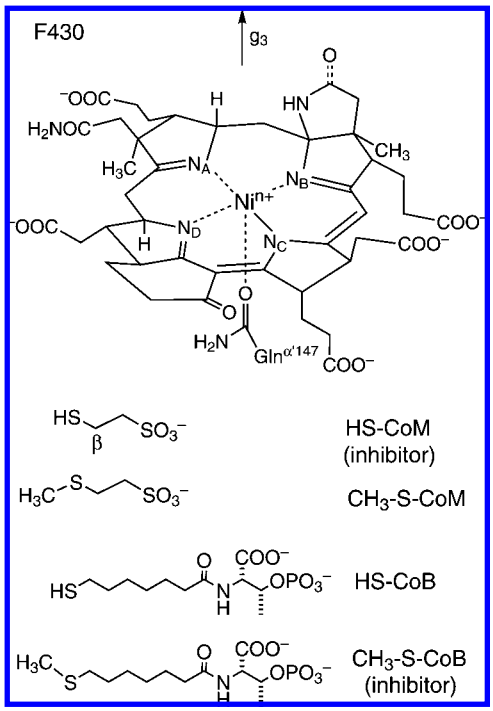

[a] Has a highly reduced tetrapyrrole macrocycle having only a small conjugated area.[2,3] The orientation of the axis $\mathbf{g}_3$ is shown. Shown below are the competitive inhibitor HS-CoM (β position indicated), substrates CH_3-S-CoM and HS-CoB, and CH_3-S-CoB (inhibitor).

group (via the ^{14}N interaction) to the nickel ion from the distal face. Figure 7 depicts the low frequency (<6 MHz) region of X-band HYSCORE spectra recorded from an $MCR_{red1/red2}$ sample at field positions where there are (A) signals only from $MCR_{red2a/red2r}$, (B) signals only from $MCR_{red1c/red2a}$, and (C) signals from $MCR_{red2a/red2r/red1c}$. The HYSCORE spectrum in Figure 7A shows only cross-peaks stemming from couplings to ^{13}C in natural abundance (indicated by the antidiagonal line at ~3.5 MHz) and a peak on the diagonal line indicated by the arrow. This probably belongs to the lactam ring nitrogen with $A(^{14}N) \approx 0$ MHz (hence it is on the diagonal) as discussed below. In Figure 7B there are two new intense cross-peaks, indicated by the arrows, that can be satisfactorily simulated with a weakly coupled nitrogen having the hyperfine coupling, $|A(^{14}N)| \approx 0.5$ MHz, and nuclear quadrupole parameters of $|e^2qQ/h| \approx 2.5$ MHz and $\eta \approx 0.3$ (see Figures S6 and S7 for the measurement set). This coupling can be assigned to either the MCR_{red1c} or the MCR_{red2a} state, which are the only states contributing at the field position of Figure 7B. Since there is an isotropic contribution to the hyperfine interaction, there is a delocalization of the spin density onto this nitrogen, implying coordination of the structure (containing the ^{14}N nucleus) to the paramagnetic center. There are two possible assignments: either to the lactam ring of F_{430}, which has an NH nitrogen, or to the NH_2 nitrogen bound to the oxygen of $Gln^{\alpha'147}$. A comparison of the NQI parameters to those of model compounds[45] suggests that the most likely assignment is to the NH_2 of the $Gln^{\alpha'147}$ residue. Glutamine and asparagine NH_2 nitrogens have $|e^2qQ/h| \approx 2.6-2.8$ MHz, $\eta \approx 0.3-0.4$,[46–48] whereas the HN nitrogen of histidine and proline have $|e^2qQ/h| \approx 1.4-1.7$ MHz, $\eta \approx 0.6-1.0$,[49] or the HN nitrogen of guanine has $|e^2qQ/\eta| \approx 2.63$ MHz, $\eta \approx 0.60$. Our parameters are closest to the model data from glutamine.[50] Additionally, HYSCORE data from free $Ni(I)F_{430M}$ do not show these features,[51] and the $Gln^{\alpha'147}$ residue coordinated to the nickel ion via the oxygen would be expected to have a small isotropic nitrogen hyperfine interaction. We thus tentatively assign this coupling to the NH_2 group of $Gln^{\alpha'147}$. Significantly these ^{14}N cross-peaks are absent in the $MCR_{red2r/red2a}$ states (Figure 7A). To further clarify this absence for the MCR_{red2r} state, a HYSCORE spectrum at a field position close to g_3 of MCR_{red2r} was sought. However, this required filtering out signals from $MCR_{red2a/red1c}$, since at this position $MCR_{red2r/red2a/red1c}$ states all contribute. Filtering was possible with T_1 relaxation time-filtered HYSCORE (REFINE),[52] since $T_{1,red2r}$ is significantly different from $T_{1,red2a} \approx$

(45) Grimaldi, S.; MacMillan, F.; Ostermann, T.; Ludwig, B.; Michel, H.; Prisner, T. *Biochemistry* **2001**, *40*, 1037–1043.
(46) Lendzian, F.; Rautter, J.; Käss, H.; Gardiner, A.; Lubitz, W. *Ber. Bunsen-Ges. Phys. Chem.* **1996**, *100*, 2036–2040.
(47) Spoyalov, A. P.; Hulsebosch, R. J.; Shochat, S.; Gast, P.; Hoff, A. *Chem. Phys. Lett.* **1996**, *263*, 715–720.
(48) Deligiannakis, Y.; Hanley, J.; Rutherford, A. W. *J. Am. Chem. Soc.* **1999**, *121*, 7653–7664.
(49) Hanley, J.; Deligiannakis, Y.; MacMillan, F.; Bottin, H.; Rutherford, A. W. *Biochemistry* **1997**, *36*, 11543–11549.
(50) Garcia, M. L. S.; Smith, J. A. S. *J. Chem. Soc. Perkin Trans II* **1983**, 1401–1408.
(51) Hinderberger, D.; Ebner, S.; Mayr, S.; Jaun, B.; Reiher, M.; Goenrich, M.; Thauer, R. K.; Harmer, J. *J. Biol. Inorg. Chem.* (submitted).

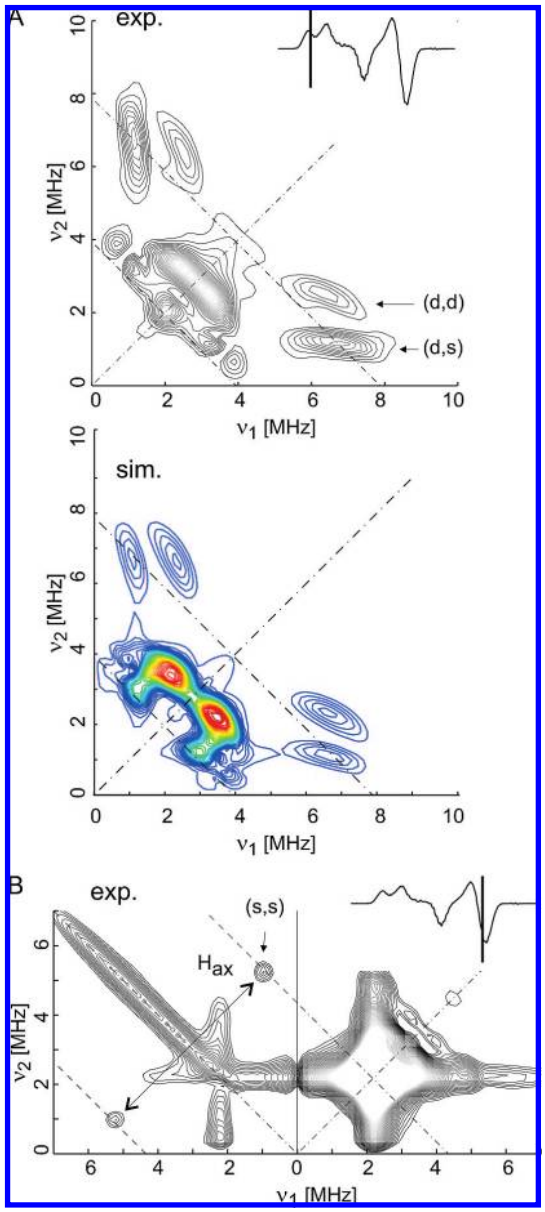

Figure 3. X-band (9.677 GHz) HYSCORE spectra measured at 20 K from an $MCR_{red1/red2}$ sample with ^2H_2O. (A) g_1 of MCR_{red2r} (301.4 mT), (B) $g_{1,2}$ of MCR_{red2a} (332.4 mT). Insets: EPR spectra showing the field positions (horizontal lines) at which the HYSCORE spectra were measured. Indicated on the graph are ^2H cross-peaks from single-quantum (s) transitions (with $\Delta m_I = \pm 1$), and double-quantum (d) transitions. The simulation (sim.) for H_{rh} is shown for experiment A.

$T_{1,red1c}$. The unfiltered HYSCORE spectrum shown in Figure 7C displays the ^{14}N cross-peaks tentatively assigned to the carboxamide nitrogen of $Gln^{\alpha'147}$ in the MCR_{red1c} state. The REFINE HYSCORE experiment measured at the same field position, but with most of the $MCR_{red1c/red2a}$ state filtered out, is shown in Figure 7D. There, it becomes apparent that the MCR_{red2r} state does not feature the weak ^{14}N signals. The inset in Figure 7C and D shows an echo-detected (pseudomodulated) EPR spectrum before and after the T_1 filtering and demonstrates that the $MCR_{red2a/red1c}$ signals are effectively (>90%) removed. These data are a strong indication that in the MCR_{red2r} state the nitrogen of $Gln^{\alpha'147}$ is more distant from the nickel center or that the carboxamide is even no longer coordinated. Tentatively

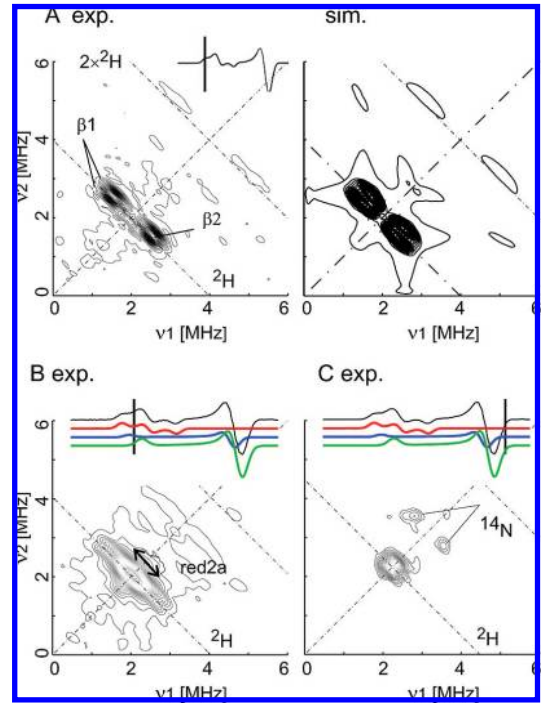

Figure 4. X-band (9.78 GHz) HYSCORE spectra measured at 20 K of $MCR_{red1/red2}$ induced with [2-$^2H_2$] HS-CoM. The antidiagonal lines drawn at $\nu(^2H)$ and $2 \times \nu(^2H)$ identify single- and double-quantum deuterium cross-peaks, respectively. Insets show the echo-detected EPR spectrum (first derivative), and positions of the HYSCORE measurements in (B and C), simulations for the components are given; MCR_{red2r} (top, red), MCR_{red2a} (middle, blue), MCR_{red1c} (bottom, green). (A) At a field position of only MCR_{red2r} signals (g_1, 305.3 mT), experiment (exp.) and simulation (sim.). Signals assigned to the nuclei $\beta 1$ and $\beta 2$ are labeled. (B) At a field position where MCR_{red2r} and MCR_{red2a} contribute (no MCR_{red1c}). Indicated are signals assigned to β nuclei of MCR_{red2a}. (C) At a field position where only MCR_{red1c} contributes. The signals labeled ^{14}N are discussed in Figure 7.

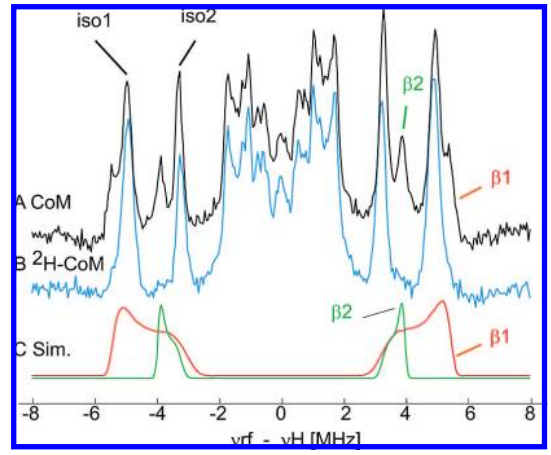

Figure 5. Q-band (34.84 GHz) Davies ENDOR spectra measured at 20 K at observer position g_1 (1087 mT) of MCR_{red2r}. (A) HS-CoM, (B) [2-$^2H_2$] HS-CoM, and (C) simulations for the $\beta 1$ and $\beta 2$ protons.

the same conclusion can be drawn for MCR_{red2a}, but this is only based on the observation at one field position.

The four hydropyrrole nitrogen hyperfine interactions in MCR_{red2a} are in the range ca. 22−38 MHz as estimated from X-band ENDOR and CW EPR data (see Figure S2). In contrast to MCR_{red2r}, we found no evidence for a much weaker hydropyrrole nitrogen interaction (using Q-band HYSCORE,

(52) Maly, T.; Prisner, T. F. *J. Magn. Reson.* **2004**, *170*, 88–96.

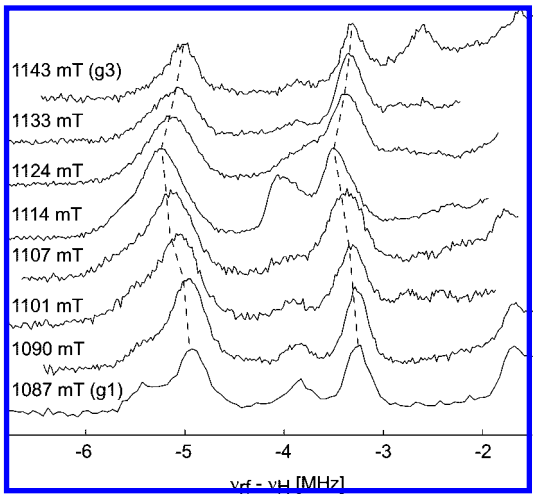

Figure 6. Q-band (34.84 GHz) Davies ENDOR spectra of a $MCR_{red1/red2}$ sample measured at 20 K at field positions corresponding to the g_1 to g_3 position of the MCR_{red2r} state. The two dashed lines follow the field dependence of the quasi-isotropic protons iso1 and iso2. For clarity only one of the electron spin manifolds is shown (low frequency side of ν_{1H}).

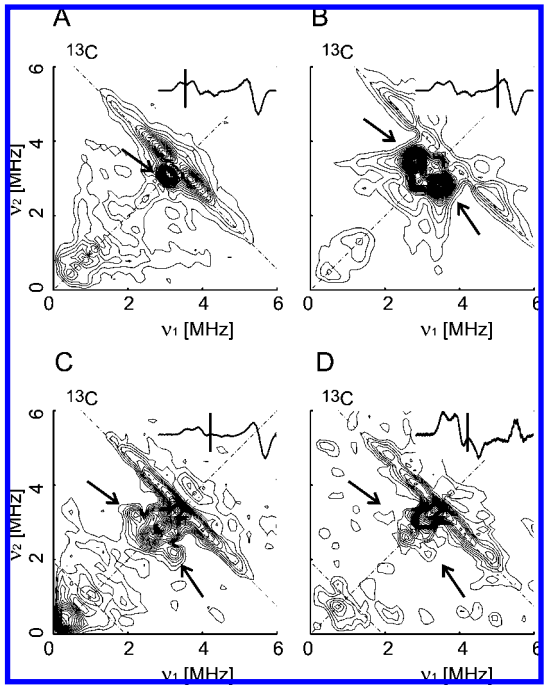

Figure 7. X-band HYSCORE spectra of $MCR_{red1/red2}$ measured at 20 K. Insets show the EPR spectrum and the field positions of the HYSCORE measurements. (A) Field position where only $MCR_{red2r/red2a}$ contribute to the HYSCORE spectrum. The marked peak probably originates from the lactam ring nitrogen. (B) Field position where only MCR_{red1c} contributes to the HYSCORE spectrum. The cross-peaks assigned to ^{14}N of $Gln^{\alpha'147}$ are indicated with the two arrows. (C) Field position where $MCR_{red1c/red2a/red2r}$ contribute to the HYSCORE spectrum. Cross-peaks assigned to ^{14}N of $Gln^{\alpha'147}$ are indicated with the two arrows. (D) Same field position as (C) but with a T_1 filter to remove $MCR_{red1c/red2a}$ contributions. ^{14}N peaks observed in (C) are suppressed below the noise level. The T_1-filtered EPR spectrum (inset) indicates that residual $MCR_{red1c/red2a}$ signals are <10%.

data not shown), indicating that, in MCR_{red2a}, there is no significant spin density anisotropy in the F_{430} macrocycle.

Discussion

Structural Proposal for MCR_{red2a}. The state MCR_{red2a} is distinguished by a nearly axial proton hyperfine interaction with a large isotropic (Fermi contact, $a_{iso} = -30$ MHz) and dipolar ($T = [-13, -12, +25]$ MHz) part, with the principal axis pointing along the g_3 axis (Scheme 2). The dipolar part T indicates that the proton is very near to the nickel ion, as can be appreciated by using the point−dipole model to calculate an electron−proton distance,[53]

$$\mathbf{T} = \sum_k \mathbf{R}_k(\alpha,\beta,\gamma) T_k diag(-1,-1,2) \mathbf{R}_k^{\dagger}(\alpha,\beta,\gamma)$$

$$\text{with } T_k = (\mu_o/4\pi h)(g_e\beta_e g_n\beta_n)\rho_k \frac{1}{r_k^3} \quad (3)$$

where r_k is the distance between the unpaired electron and the kth nucleus with spin population ρ_k, and $\mathbf{R}_k(\alpha,\beta,\gamma)$ is the rotation matrix transforming the kth point−dipole interaction into the g-matrix principal axis system. $\mathbf{T}$ is the dipolar matrix. The spin populations ρ_k on the four pyrrole nitrogens were estimated from the nitrogen hyperfine couplings as $\rho_N \approx 0.025-0.045$. Assuming the remaining part of the spin population resides on the nickel ion gives an estimate of $\rho_{Ni} \approx 0.90-0.82$, in line with a metal centered complex. These values are consistent with DFT results discussed later. Using this five-center model and a model structure for F_{430} (atom positions in Scheme 2A), eq 3 gives a distance $r_{Ni-Hax} = 0.173-0.179$ nm. Even though the point−dipole model applied to a proton so close to the nickel has limited accuracy (since here the spin population can not be accurately treated as five points), this back of the envelope calculation shows that proton H_{ax} is so strongly coupled to the unpaired electron that the only reasonable conclusion is that the MCR_{red2a} state contains a paramagnetic nickel hydride complex. This assertion is further supported by DFT data (see below) and by comparison to the Ni(III) hydride complex in H_2-sensing NiFe hydrogenase with $A(^1H) = -3.5 + [-14.5, -7.3, 21.9]$ MHz.[54] In this only example of a paramagnetic formally Ni(III) hydride we found in the literature, the isotropic part of the proton hyperfine interaction (−3.5 MHz) is quite different from our case (−30 MHz) because the unpaired electron in the hydrogenase resides predominantly in the nickel d_{z^2} orbital and the proton is located near the nodal plane of d_{z^2}, whereas in MCR_{red2a} the unpaired electron resides in the $d_{x^2-y^2}$ orbital which polarizes the d_{z^2} orbital leading to a large isotropic coupling on the proton located along the z-axis. However, the proton dipolar coupling is very similar in MCR_{red2a} and NiFe hydrogenase. On the basis of DFT calculations, Lubitz and coworkers report a Ni−H distance of ca. 0.163 nm, whereas the point−dipole model employing a spin population of $\rho_{Ni} = 0.6$ gave 0.172 nm.

As discussed above, the ^1H (^2H) hyperfine couplings to the β-CH_2 (β-C^2H_2) nuclei indicate that coenzyme M is closer to the nickel in MCR_{red2r} than in MCR_{red1c} and MCR_{red2a}. Whereas we have shown earlier that in MCR_{red2r} the sulfur of HS-CoM is coordinated to the nickel, the corresponding information on the Ni−S distance for MCR_{red2a} is not available yet. Therefore, one has to consider a range of bonding situations for the formal Ni hydride in MCR_{red2a}: from a true Ni(III) hydride without contact between the hydrogen and the sulfur of $^-$S-CoM to an agostic type bond between Ni and H-SR and, eventually, a weak hydrogen-bond-like interaction between Ni(I) and the proton of the sulfhydryl group of HS-CoM. Because the only restriction with regard to the origin of the strongly coupled proton is that

(53) Pöppl, A.; Kevan, L. *J. Phys. Chem.* **1996**, *100*, 3387–3394.
(54) Brecht, M.; van Gastel, M.; Buhrke, T.; Friedrich, B.; Lubitz, W. *J. Am. Chem. Soc.* **2003**, *125*, 13075–13083.

Scheme 2[a]

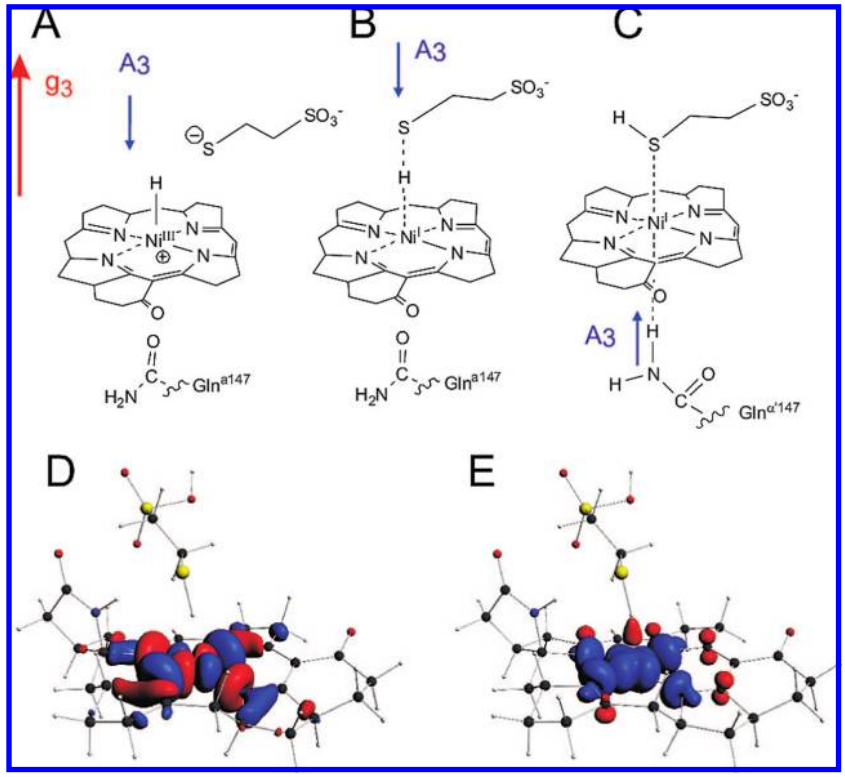

[a] (A−C) Schematic representation of the DFT models investigated to explain the EPR parameters of MCR_{red2a}, the axes g_3 and A_3 of H_{ax} are indicated. The lactam ring has been removed for clarity. In (A) and (C), $^{-}$S-CoM and HS-CoM, respectively, are not coordinated to the nickel and are not included in the DFT calculations but shown to indicate that the molecules are close to the paramagnetic center. (D) Singly occupied molecular orbital (SOMO). (E) Spin density: blue, positive; red, negative as calculated for structure B.

it must be exchangeable with solvent protons, one also has to consider the OH protons on the two tyrosine residues in the active site and the NH_2 protons of the carboxamide group of the distal ligand $Gln^{\alpha'147}$.

To aid the interpretation of the experimental data, three model complexes featuring a nickel hydride (Scheme 2) were investigated by calculating the optimized geometric structure and EPR parameters using density functional theory (DFT). A comprehensive list of EPR and structure parameters calculated by DFT are given in Tables S1−S12 and Figures S8−S14. Model complex 2A, $[H-Ni^{III}F_{430}]^{+1}$, with no interaction between the Ni-bound hydrogen and other ligands (i.e., $^{-}$S-CoM), has an extremely short calculated Ni−H distance of $r_{calc,Ni\text{-}Hax} = 0.144$ nm (Figure S8), leading to a calculated proton hyperfine coupling of $A_{calc}(^1H) = -56.1 + [-18.4, -16.4, 34.8]$ MHz with both the isotropic and dipolar parts twice as large as the experimental coupling ($A_{exp} = -30 + [-13, -12, 25]$ MHz).[55] An extended model with a distal axial $Gln^{\alpha'147}$ ligand was almost identical in terms of the dipolar part but shows a larger negative calculated $A_{iso,calc}$ ($r_{calc,Ni\text{-}Hax} = 0.143$ nm, $r_{calc,Ni-O} = 0.211$ nm, $A_{iso,calc} = -124$ MHz). The short $Ni-H_{ax}$ bond length found in the minimized structures 2A may be due to an environmental effect not taken into account by the DFT calculation, such as an electrostatic interaction between the proton and a negative charge on $^{-}$S-CoM. Model complex 2B, $[(CoM\text{-}S\text{-}H)\text{-}NiF_{430}]^0$, has $r_{calc,Ni\text{-}Hax} = 0.200$ nm and a hyperfine coupling $A_{calc}(^1H) = -6.7 + [-7.3, -7.0, 14.3]$ MHz which is significantly smaller than the experimental data (Figure S9). To search for an agreement between experimental and DFT results for the *dipolar part* of the hyperfine coupling, we moved the H-S-CoM ligand in the range $r_{Ni\text{-}Hax} = 0.16-2.0$ nm along the $Ni-H_{ax}$ vector and calculated by DFT the EPR parameters for each distance. The DFT (Figure S10) and experimental dipolar hyperfine coupling match for a Ni−H distance of $r_{Ni\text{-}Hax} = 0.166$ nm, with an $A_{iso,cal} = -12.1$ MHz with the expected negative sign. This distance derived from the dipolar part of the DFT hyperfine calculation with $r_{Ni\text{-}Hax} = 0.166$ nm is in satisfactory agreement with our estimate from the point−dipolar calculation using eq 3 of 0.173−0.179 nm. The fact that the $Ni-H_{ax}$ distance consistent with the experimental dipolar coupling lies between the two geometry optimized gas phase structures in Scheme 2A/2B could result from constraints not included in the DFT model (e.g., binding of the SO_3^- group of HS-CoM to the arginine residue in the protein whereas in the DFT model this group is unconstrained). Our model 2B yields small DFT calculated hyperfine couplings (<4 MHz, Table S2) to the β protons in satisfying agreement with the experimental EPR data.

Simulation of a very weak, hydrogen bond-like interaction between the SH group and $Ni(I)F_{430}$ could not be performed by DFT geometry optimization in the gas phase, because it is not a minimum in the absence of retaining forces from the protein environment. Analogous axial interactions between acidic protons (N−H) and Pt(II) in a square planar environment have been observed by NMR and X-ray structural analysis and

(55) We divide the hyperfine coupling into an isotropic part $a_{iso} = (A_1 + A_2 + A_3)/3$ and a dipolar part $[T_1, T_2, T_3] = [A_1, A_2, A_3] - a_{iso}$. The dipolar part depends upon the spin density distribution and should be well predicted by DFT. The isotropic part will not be accurately calculated by the DFT implemented here and can have a considerable error.

were described as "remote" or "remote agositic".[56] However, the corresponding metal−hydrogen bond lengths in these complexes are distinctly longer (0.22 nm) than the distance for MCR_{red2a} derived here from EPR data. A nearly isotropic hyperfine interaction (A = 13 MHz), much weaker than that in MCR_{red2a}, has been observed between the Ni(I) of free coenzyme F_{430} in frozen aqueous solution and the hydrogen of solvent water by electron spin echo envelope modulation (ESEEM) spectroscopy.[57]

Scheme 2 shows the calculated SOMO (D) and spin density distribution (E) of the geometry optimized complex 2B [CoM-S-H-NiF_{430}]^0 (minimized structure with Ni−H_{ax} = 0.200 nm). The SOMO has a high nickel $d_{x^2-y^2}$ character with negligible mixing with the d_{z^2} orbital and has no direct contributions from the thiol proton of the HS-CoM ligand. The spin density on the strongly coupled proton is large and negative and arises by spin polarization, consistent with bonding overlap between the Ni d_{z^2} and hydrogen orbitals. However, the DFT calculations predict an $A_{iso}(H_{ax})$ value that is smaller than the experimentally determined one at the (imposed) Ni−H_{ax} distance of 0.166 nm, where the dipolar couplings from DFT fit the experimental ones best; the $A_{iso}(H_{ax})$ predicted by DFT (−12 MHz) is ca. half of the experimental value (−30 MHz). The magnitude of this coupling and of the negative spin density are very sensitive to any $d_{z^2}/d_{x^2-y^2}$ mixing, i.e., to small structural changes (c.f. the effect of the axial glutamine ligand, Table S1). Since the nature of the conformational change of the protein upon binding of coenzyme B is still unknown, the geometry optimized gas phase models 2A and 2B we had to resort to for the DFT calculations are certainly only approximations to the actual larger structure. Therefore and because particularly the calculation of isotropic hyperfine coupling constants in transition metal complexes by DFT methods carries a sizable error presently,[58–60] we consider the agreement of calculations and experiment as satisfactory and the electronic structure provided by DFT as a model which conveys the essential feactures.

Qualitatively, the bonding situation in MCR_{red2a} can be described as an agostic Ni−H bond involving interaction of the full nickel d_{z^2} orbital with the σ^* orbital of the H−S bond. Another possible interpretation of this bond would be that of a hydrogen bond between the acidic S−H proton and the d_{z^2} lone pair on the nickel.

Scheme 2C considers the possibility that the coordinated hydrogen originates from the NH_2 group of the glutamine α′147 residue. DFT calculations yield a r(Ni−S) = 0.400 nm, r(Ni−H) = 0.236 nm, and small proton hyperfine couplings compared to the experiment, $A_{calc}(^1H) = -0.5 + [-4.6, -4.6, 9.2]$ MHz, suggesting this type of structure can be ruled out (Figure S11). An extended Scheme 2C with $^-$S-CoM instead of HS-CoM gives very similar results with respect to the glutamine α′147 residue coordination (r(Ni−H) = 0.235 nm, $A_{calc}(^1H) = -1.4 + [-4.9, -4.5, 9.4]$ MHz) but has a much shorter distance to the sulfur r(Ni−S) = 0.269 nm.

In summary we consider Scheme 2A and B as a suitable model for the coordination environment around the nickel ion in MCR_{red2a}.

Structural Proposals for MCR_{red2r}. Previous investigations have shown that in the MCR_{red2r} state the thiol(ate) S of HS-CoM is directly coordinated to the nickel ion, and the four hydropyrrole nitrogen hyperfine couplings indicate a significant asymmetry in the spin population on the macrocycle ($\rho_{N_B,N_C,N_D} \cong 0.035$, $\rho_{N_A} \cong 0.015$). The sulfur hyperfine coupling of $|A(^{33}S)| = [15,15,35]$ MHz indicates a spin population on the sulfur of $\rho_S \cong 0.08$ or $\cong 0.17$, depending on the relative sign of the principal values.[31] To use eq 3 (see later) we need the nickel spin population which we estimate as $\rho_{Ni} \approx 0.70-0.80$ by requiring that the total spin population sums to 1. This value is qualitatively consistent with the experimental ^{61}N hyperfine coupling of $A(^{61}Ni) = [39, 44, 67]$ MHz.[22] We thus have six centers to describe the spin population distribution.

The "unusual" g-values of MCR_{red2r} are very different from those of the $MCR_{red1/ox1}$ states or five- and six-coordinated nickel(I) and nickel(III) model complexes.[61,62] However, the g-values of MCR_{red2r} are very similar to some Ni(I)(STPP) complexes (STPP = 5,10,15,20-tetraphenyl-21-thiaporphyrin) where the nickel is equatorially coordinated to three nitrogens and one sulfur ligand of the macrocycle,[63] the pentacoordinated nickel complex Ni(I)(DAPA)$(SPh)_2$ (DAPA=2,6-bis[1-(phenylimino)ethyl]pyridine) with two thiolate ligands in the equatorial plane and three nitrogens of the DAPA ligand occupying the remaining coordination sites,[64] and the Ni(III) tetraphenylcarbaporphyrin, Ni(III)(CTPP), an inverted porphyrin where the nickel ion is coordinated to three nitrogens and one carbon in the porphyrin plane.[65] In the case of Ni(I)(STPP) the rhombic g matrix is attributed mainly to the axial ligands, rather than to the replacement of one of the pyrroles by a thiophene; the complex Ni(I)(STPP)(SO_2) has nearly axial g values, whereas Ni(I)(STPP)$(2,4\text{-}Me_2py)_2$ with two axial 2,4-lutidine ligands has g values very close to those of MCR_{red2r}. A similar behavior is observed for the Ni(III)(CTPP) complexes, where again depending on the axial ligands, the g values reflect approximately tetragonal symmetry or can be highly rhombic (attributed to a ground state described as a linear combination of $d_{x^2-y^2}$ and d_{z^2} orbitals).

The β proton data together with the point−dipole model of eq 3 and a six-center spin population distribution (4 × N, S, and Ni) were used to estimate the position and orientation of the two β nuclei with respect to the paramagnetic center. This was achieved by optimizing the position of HS-CoM relative to F_{430}. A good fit to the experimental dipolar hyperfine couplings of protons $\beta 1$ and $\beta 2$ is obtained for Ni ↔ H_β distances of $r_{\beta 1} = 0.28(0.02)$ nm and $r_{\beta 2} = 0.38(0.02)$ nm (mean calculated dipolar hyperfine couplings $T_{\beta 1} = [-3.6, -3.1, 6.7]$ MHz and $T_{\beta 2} = [-1.5, -1.3, 2.8]$ MHz). The EPR distances are very similar to the values $r_{\beta 1} = 0.30$ nm and $r_{\beta 2} = 0.42$ nm calculated from the Ni(II) $MCR_{ox1\text{-}silent}$ crystal structure. The EPR distances $r_{\beta 1}$ and $r_{\beta 2}$ support the thiol(ate) ^{33}S hyperfine coupling data showing that HS-CoM is coordinated to the nickel and further indicate that the position of HS-CoM relative to F_{430} is similar to that found in the crystal structure.

(56) Albinati, A.; Lianza, F.; Pregosin, P. S.; Müller, B. *Inorg. Chem.* **1994**, *33*, 2522–2526.
(57) Holliger, C.; Pierik, A. J.; Reijerse, E, J.; Hagen, W. R. *J. Am. Chem. Soc.* **1993**, *115*, 5651–5656.
(58) Munzarová, M.; Kaupp, M. *J. Phys. Chem. A* **1999**, *103*, 9966–9983.
(59) Neese, F. *Curr. Opin. Chem. Biol.* **2003**, *7*, 125–135.
(60) Neese, F. *J. Biol. Inorg. Chem.* **2006**, *11*, 702–711.
(61) Salerno, J. C., Lancaster, J. R., Jr., Eds. *The Bioinorganic Chemistry of Nickel*; VCH Publishers: Deerfield Beach, FL 1988; pp 53−102..
(62) Pinho, D.; Gomes, P.; Freire, C.; de Castro, B. *Eur. J. Inorg. Chem.* **2001**, *6*, 1483–1493.
(63) Chmielewski, P.; Grzeszczuk, M.; Grazynski, L. L.; Lisowski, J. *Inorg. Chem.* **1989**, *28*, 3546–3552.
(64) Marganian, C. A.; Vazir, H.; Baidya, N; Olmstead, M. M.; Mascharak, P. K. *J. Am. Chem. Soc.* **1995**, *117*, 1584–1594.
(65) Chmielewski, P. J.; Grazynski, L. L. *Inorg. Chem.* **1997**, *36*, 840–845.

Scheme 3[a]

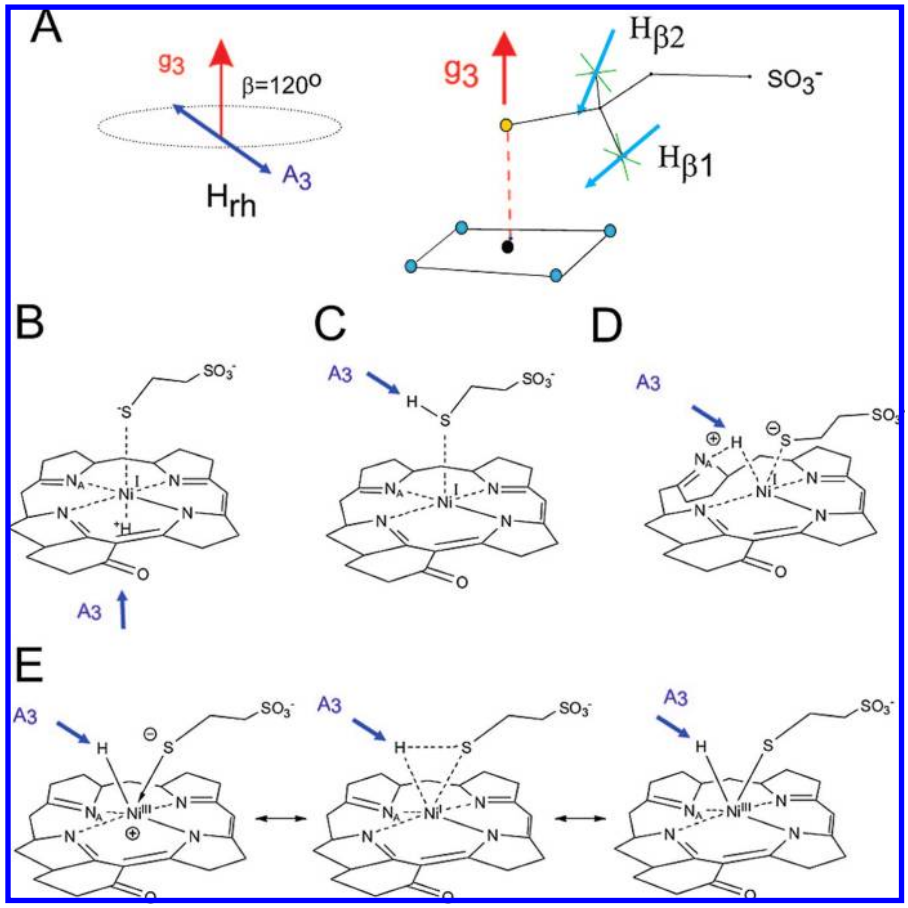

[a] (A) Schematic representation of the experimental hyperfine interactions for the β protons and the exchangeable proton H_{rh}. The lactam ring has been removed for clarity. The g_3 axis is along the Ni−S bond, and the principal axis (A_3) of each hyperfine interaction is shown as a red line. The A_3 axis of H_{rh} is tilted by 120° from g_3; however the orientation relative to the plane of F_{430} is unknown (Ni−S bond direction is unknown). Solid balls show the 6 spin population centers used in eq 3. DFT models for (B) hydride from distal face, (C) HS-CoM coordinates as a thiol, an unlikely structure, and (D) H_{rh} bound to N_A of F_{430}. (E) Hydride with three resonance structures (schematic proposal, not DFT optimized structure).

The exchangeable proton H_{rh} has an hyperfine interaction with a large isotropic (Fermi contact) ($|a_{iso}| = 20$ MHz) and a large dipolar ($T = \pm[-9,-6,15]$ MHz) part, showing that H_{rh} is close to the paramagnetic center, i.e., either directly coordinated to the nickel, bound directly to the coordinated sulfur, or bound to one of the four hydropyrrole nitrogens. Other possible protons, like the two amide protons of $Gln^{\alpha'147}$ (assuming the X-ray structure) or the NH proton from the lactam ring of F_{430}, are at a distance of >0.3 nm from the nickel for which a point−dipole calculation (eq 3) shows that the predicted dipolar hyperfine couplings ($T_{cal} < [-2.5, -2.5, 5]$ MHz) are far too small to explain the experimental couplings. Experimentally, the principal dipolar axis of H_{rh} is tilted by 120° from the g_3 axis which is approximately along the Ni−S bond (Scheme 3A).[66]

Possible structural candidates for MCR_{red2r} are shown in Scheme 3. Structures with a hydride ligand coordinated to either the distal (B) or proximal face (E) (two *cis*-ligands; $^-$S-CoM and H_{rh}) of F_{430} were considered. However, the *trans*-complex B would have the principal dipolar axis pointing along the g_3 axis, which is inconsistent with the experimentally derived angle and allows B to be ruled out. B is however a possible candidate for MCR_{red2a} (DFT calculations give r(Ni−H) = 0.147 nm and r(Ni−S) = 0.240 nm, Figure S12). Scheme 3C corresponds to a thiol coordinated to Ni^IF_{430} via sulfur. Using eq 3 with the spin population distribution derived above, a match to the experimental dipolar hyperfine coupling is only obtained with a S−H distance of r(S−H) = 0.13 nm and a $\rho_S = 0.17$ ($T_{cal} \approx [-8,-7,14]$ MHz, r(Ni−S) = 0.22 nm). With $\rho_S = 0.08$ the calculated dipolar hyperfine coupling would be far too small ($T_{cal} \approx [-5,-4,9]$ MHz). In addition the calculated structure (Figure S13) has $r_{Ni-S} = 0.396$ nm and a correspondingly small thiol proton hyperfine coupling $A_{cal} = -2.0 + [-0.5, -0.5, 1]$ MHz. Experimental studies show that the nickel(I) form of free coenzyme F_{430} pentamethyl ester in noncoordinating solvents does not coordinate to thiols or thiolates. Therefore and because it is difficult to reconcile the very pronounced g-matrix rhombicity of MCR_{red2r} with a single weak axial ligand, we rule Scheme 3C out.

Scheme 3D and 3E consider a distortion of F_{430}, inspired by the experimental g-values and nitrogen hyperfine couplings, that would be triggered by a conformation change upon HS-CoB binding. To model such a conformation change would require a very large model (at least a shell around HS-CoB, HS-CoM and F_{430}) and since there is presently insufficient experimental data to limit the search space, we have not attempted a calculation. Thus 3E and 3D focus on the immediate coordination environment around the nickel ion and are potentially capable of explaining the experimental EPR data but remain

(66) This is based on experimental data showing that the direction of the largest ^{33}S and ^{61}Ni hyperfine couplings are along g_3.

Scheme 4. Proposal for the Critical Bond Activation Step in MCR with the Substrates CH_3-S-CoM and HS-CoB, Inspired by Parallels to the red2 and BPS/BrMe States of MCR

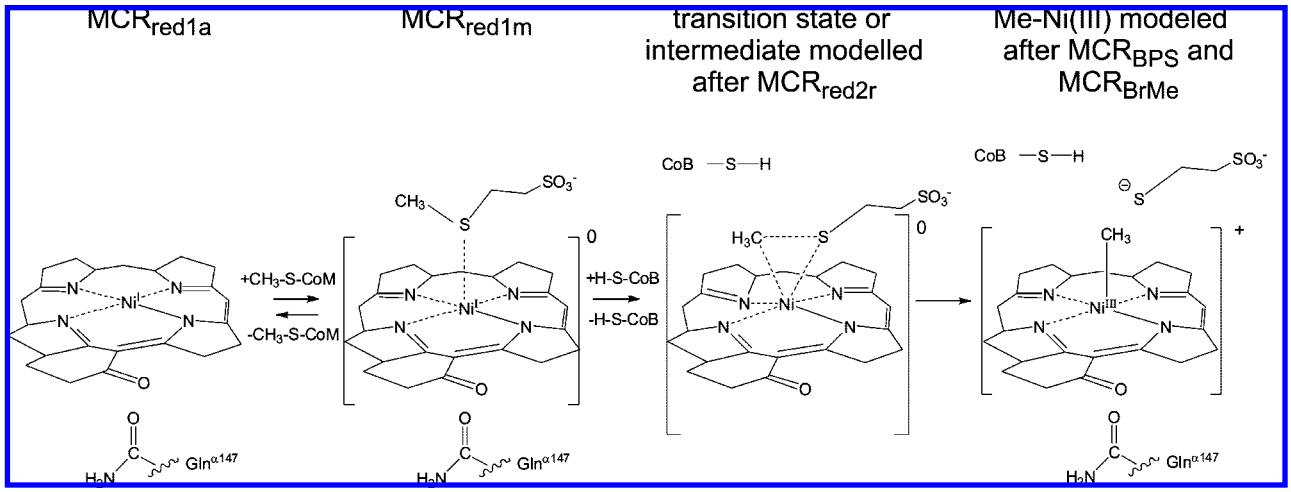

highly speculative. Structure 3E is formally the result of an oxidative addition of a S−H bond to $Ni^{I}F_{430}$ giving a (S)(H)-$Ni^{III}F_{430}$ species. The concurrent binding of an electrophile (H^+) and a thiolate to nickel is expected to be energetically more favorable than axial coordination of a single strong donor ligand such as thiolate. The model is predicted to exhibit a dipolar hyperfine coupling from the electrophile H_{rh} consistent with the experimental data for a nickel distance of $r_{Ni\text{-}Hrh} \cong 0.19-0.21$ nm (application of eq 3 using the six-center experimental spin population distribution). The conceptual problem with structures such as E is that, to our knowledge, there is no precedence for *cis*-coordination of two ligands to one face of a tetraazamacrocyclic nickel complex with four strong equatorial ligands in a square planar arrangement. In this context, the experimental observation that at least one hydropyrrolic nitrogen in MCR_{red2r} shows a much weaker hyperfine coupling than the others is particularly noteworthy. Together with the disappearance of the weak ^{14}N coupling attributed to the distal axial carboxamide ligand when MCR_{red1c} is transformed into MCR_{red2r}, this could indicate that one of the rings (most probably ring A) of the hydrocorphin is tilted out of the plane and that the corresponding nitrogen displaces the axial glutamine ligand and coordinates weakly in a side-on direction, similar to the coordination of the thiophene sulfur in Ni(STTP) (see structures E in Scheme 3). It must also be pointed out that we could not calculate a geometry optimized structure for Scheme 3E; all our attempts converged toward Scheme 3C/D.

A further possibility based on the geometric constraints derived from our EPR data would be a structure such as Scheme 3D where the strongly coupled H_{rh} is in a bridging position between the Ni and one of the hydropyrolic nitrogens with the latter moved out of the plane of the macrocycle.[67,68] Our optimized structure (Figure S14) has $r_{Ni\text{-}Hrh} = 0.224$ nm, $r_{Hrh\text{-}N} = 0.105$ nm. The calculated hyperfine coupling for H_{rh}, $A_{cal} = +2.2 + [-7.0, -2.6, 9.6]$ MHz, has a similar dipolar part as found experimentally but a significantly smaller isotropic value.

MCR_{red2} States as Potential Models for Intermediates in the Catalytic Cycle. Addition of HS-CoM to active MCR_{red1a} results in the MCR_{red1c} state where the thiol(ate) sulfur has a very weak interaction with the Ni^{I} ion. HS-CoM is thus positioned to interact with the nickel upon addition of the second substrate HS-CoB (or CH_3-S-CoB). Positioning of the thiol(ate) sulfur (or in the natural substrate the thioether sulfur of CH_3-S-CoM) above the nickel of F_{430} is facilitated in the enzyme by a pocket wherein the SO_3^- group is bound to an arginine residue in the protein. Upon addition of either HS-CoB or CH_3-S-CoB the state MCR_{red1c} is partially converted into a hydride complex (MCR_{red2a}, axial EPR spectrum) and into a complex in which the tetra-azamacrocycle is geometrically or electronically strongly distorted, the sulfur of CoM is coordinated to the nickel, and a hydrogen is close to the metal (MCR_{red2r}, rhombic EPR spectrum). This leads us to propose the reaction scheme presented in Scheme 4 for the critical S−C activation step in the catalytic cycle with the physiological substrate CH_3-S-CoM. MCR_{red1c} is analogous to MCR_{red1m}, with HS-CoM replacing CH_3-S-CoM. MCR_{red2a} is analogous to the $CH_3-Ni^{III}F430$ species which is known to be stable in the active site[15,17,18] and corresponds to an intermediate in the catalytic cycle proposed by Jaun and Thauer. Formally the nickel hydride [CoM-S···H−$Ni^{III}F_{430}$] and the cation complex $[CH_3-Ni^{III}F_{430}]^+$ can be described as products of an oxidative addition of either H^+ of CH_3^+ to the filled d_{z^2} nickel orbital, leaving the unpaired electron in predominately a $d_{x^2-y^2}$ orbital as can be seen from the *g* values and strong pyrrole ^{14}N hyperfine interactions. MCR_{red2r} is potentially a model intermediate for the activation of the C−S bond of CH_3-S-CoM, maybe involving a side-on C−S coordination to the nickel. Clearly, addition of HS-CoB is required for catalysis or to induce the MCR_{red2} states, probably resulting in a conformation change to MCR upon binding.[69] Such a conformational change may actually represent the rate limiting step in methane formation.

Conclusion

We have shown that, if the inhibitor coenzyme M is bound instead of the natural substrate, addition of coenzyme B to the active enzyme induces two new states (MCR_{red2a} and MCR_{red2r}). The structure of the species giving rise to the axial MCR_{red2a} signal as deduced from the EPR data is corroborated by the

(67) Bernard Chevrier, B; Weiss, R. *J. Am. Chem. Soc.* **1976**, *98*, 2985–2990.

(68) Callot, H. J.; Tschamber, T.; Chevrier, B.; Weiss, R. *Angew. Chem., Int. Ed.* **1975**, *14*, 567–568.

(69) We have experimental evidence, via ^{19}F ENDOR data, that a conformation change takes place upon binding of the substrate analogue CF_3-S-CoB. Manuscript in preparation.

results of DFT calculations and is intermediate between a Ni^{III}-hydride and an agostic interaction of the CoM-S-H hydrogen with Ni^{I}.

For the rhombic MCR_{red2r} signal, no structural model could be found yet that reproduces all EPR data satisfactorily when simulated by a DFT calculation. However, the EPR data reported here and earlier[29,31] constitute a set of restraints on any structural proposal for MCR_{red2r}: (a) an exchangeable proton is close to the nickel on a Ni−H vector enclosing an angle of ca. 60° or ca. 120° with the Ni−S bond; (b) the thiol sulfur of coenzyme M is coordinated to the nickel; (c) the spin density in the hydrocorphin macrocycle is much more anisotropic than that in all other MCR states, indicating a large geometric and/or electronic distortion from the quasi-tetragonal coordination found in MCR_{red1} and MCR_{red2a}; (d) the carboxamide group of $Gln^{\alpha'147}$ is no longer coordinated to the nickel from the distal side.

It is known that gaseous nickel hydrides are capable of activating methane,[70,71] e.g., $NiH^+ + CH_4 \rightarrow Ni(CH_3)^+ + H_2$ and $Ni(H)(OH)^+ + CH_4 \rightarrow Ni(CH_3)(OH)^+ + H_2$, the later reaction formally involving a paramagnetic Ni^{III} cation complex. In view of the still indirect but growing body of evidence for "reverse methanogenesis", i.e., anaerobic oxidation of methane catalyzed by Ni-hydrocorphinate-containing enzymes very closely resembling MCR,[72,73] we consider that the new nickel hydride species reported here may well play a crucial role in the activation step of methane.

Acknowledgment. A.S. passed away on January 4, 2006. We thank the Swiss National Science Foundation (SNF), the Max Planck Society, the Fonds der Chemischen Industrie, the Petroleum Research Fund, and the EPSRC and BBSRC for financial support. D.H. gratefully acknowledges a research scholarship (HI 1094/1-1) by the Deutsche Forschungsgemeinschaft (DFG).

Supporting Information Available: Figures S1 to S14 and Tables S1 to S12. This information is available free of charge via the Internet at http://pubs.acs.org/.

JA710949E

(70) Schlangen, M.; Schwarz, H. *Angew. Chem., Int. Ed.* **2007**, *46*, 5614–5617.
(71) Schlangen, M.; Schröder, D.; Schwarz, H. *Angew. Chem., Int. Ed.* **2007**, *46*, 1641–1644.
(72) Krüger, M.; Meyerdierks, A.; Glöckner, F. O.; Amann, R.; Widdel, F.; Kube, M.; Reinhardt, R.; Kahnt, J.; Böcher, R.; Thauer, R. K.; Shima, S. *Nature* **2003**, *426*, 878–881.
(73) Shima, S.; Thauer, R. K. *Curr. Opin. Microbiol.* **2005**, *8*, 643–648.
(74) Albracht, S. P. J.; Ankel-Fuchs, D.; Van der Zwaan, J. W.; Fontijn, R. D.; Thauer, R. K. *Biochim. Biophys. Acta* **1986**, *870*, 50–57.
(75) Duin, E. C.; Cosper, N. J.; Mahlert, F.; Thauer, R. K.; Scott, R. A. *J. Biol. Inorg. Chem.* **2003**, *8*, 141–148.
(76) Tang, Q.; Carrington, P. E.; Horng, Y. C.; Maroney, M. J.; Ragsdale, S. W.; Bocian, D. F. *J. Am. Chem. Soc.* **2002**, *124*, 13242–13256.
(77) Telser, J.; Davydov, R.; Horng, Y.-C.; Ragsdale, S. W.; Hoffman, B. M. *J. Am. Chem. Soc.* **2001**, *123*, 5853–5860.